

GeNeRT: A Physics-Informed Approach to Intelligent Wireless Channel Modeling via Generalizable Neural Ray Tracing

Kejia Bian, Meixia Tao, *Fellow, IEEE*, Shu Sun, *Senior Member, IEEE* and Jun Yu

Abstract—Neural ray tracing (RT) has emerged as a promising paradigm for channel modeling by combining physical propagation principles with neural networks. It enables high modeling accuracy and efficiency. However, current neural RT methods face two key limitations: constrained generalization capability due to strong spatial dependence, and weak adherence to electromagnetic laws. In this paper, we propose GeNeRT, a Generalizable Neural RT framework with enhanced generalization, accuracy and efficiency. GeNeRT supports both intra-scenario spatial transferability and inter-scenario zero-shot generalization. By incorporating Fresnel-inspired neural network design, it also achieves higher accuracy in multipath component (MPC) prediction. Furthermore, a GPU-tensorized acceleration strategy is introduced to improve runtime efficiency. Extensive experiments conducted in outdoor scenarios demonstrate that GeNeRT generalizes well across untrained regions within a scenario and entirely unseen environments, and achieves superior accuracy in MPC prediction compared to baselines. Moreover, it outperforms Wireless Insite in runtime efficiency, particularly in multi-transmitter settings. Ablation experiments validate the effectiveness of the network architecture and training strategy in capturing physical principles of ray-surface interactions.

Index Terms—Wireless channel modeling, ray tracing, deep neural network, generalization capability, ray-surface interaction.

I. INTRODUCTION

WIRELESS channel modeling serves as a fundamental prerequisite for modern communication system design. By accurately characterizing wireless radio propagation mechanisms, such as path loss, multipath fading, and delay spread, channel models drive critical processes ranging from architectural design to performance evaluation and network planning. As the sixth-generation (6G) wireless systems advance into new frontiers encompassing new spectrum bands, space-air-ground-sea integrated networks, low-altitude economy applications, and integrated communication and sensing functionalities, they demand novel channel modeling methods that simultaneously achieve high accuracy, low complexity, and strong generalization.

Conventional channel modeling methods can be divided into three major categories: stochastic channel modeling (SCM),

deterministic channel modeling (DCM), and hybrid channel modeling (HCM). SCM, including non-geometry and geometry based stochastic modeling, abstracts the random characteristics of the channel by probabilistic models [2]. This modeling approach has been widely used in standardized channel models, such as 3GPP TR 38.901 [3]. However, SCM can only provide empirical distributions of channel parameters for general scenarios and cannot provide site-specific channel characteristics. In contrast, DCM leverages deterministic methods to achieve higher accuracy and site-specific realism through map-based modeling. Typical deterministic methods are full-wave simulation [4] and ray tracing (RT) [5]. Among them, RT predicts radio wave propagation by simulating physical interactions of rays with objects in three-dimensional (3D) environments. RT is much more computationally efficient and hence widely adopted in practical wireless system design. Nevertheless, RT suffers from potentially inaccurate approximations of Maxwell's equations, particularly in complex or irregular environments. HCM combines the strengths of SCM and DCM to achieve a trade-off between accuracy and computational complexity. One popular type of HCM uses RT to construct dominant propagation paths, while employing different stochastic approaches to model the remaining components as in [6], [7]. However, the persistent dependence on statistical elements remains a constraint on the accuracy of HCM.

Recent advances in artificial intelligence (AI) have brought increasing attention to intelligent channel modeling (ICM) [8]–[12], which leverages machine learning techniques to learn environment features, thereby achieving more accurate and site-specific channel modeling. This line of work can be broadly classified into three categories. The first employs neural networks to directly map environmental features to channel characteristics in an end-to-end manner. For instance, in [13], a UNet-based convolution neural network (CNN) is employed to model and predict path loss distributions in urban environments by taking a 3D city map as input. To improve prediction accuracy in urban street canyons, the authors in [14] augment 3D building mesh data with LiDAR point cloud-based street clutter information, and adopt a CNN-based autoencoder to extract relevant spatial features. However, the aforementioned methods [13], [14] often suffer from a lack of interpretability and limited generalization capabilities.

The second category leverages wireless radiation field reconstruction techniques to predict the 3D spatial distribution of signal strength. Specifically, NeRF² in [15] introduces a voxel-

Kejia Bian is with the School of Information Science and Electronic Engineering, Shanghai Jiao Tong University, Shanghai, 200240, China, and also with the Shanghai Innovation Institute, Shanghai 200231, China (email: kejiabian2024@sjtu.edu.cn).

Meixia Tao, Shu Sun, and Jun Yu are with the School of Information Science and Electronic Engineering, Shanghai Jiao Tong University, Shanghai, 200240, China (emails: {mxtao, shusun, shjdyujun}@sjtu.edu.cn).

Part of this paper was submitted to IEEE/CIC ICC 2025 for review [1].

TABLE I: Summary of Notations.

Notation	Description
$N_{i,j,n}$	The number of propagation paths between i -th transmitter (Tx) and j -th receiver (Rx), propagation path index
$a_n, \tau_n, \Theta_n, \Phi_n, d_n, I_n$	Total attenuation coefficient, delay, azimuth/elevation angles of departure, azimuth/elevation angles of arrival, propagation distance, and total number of ray-surface interactions associated with the n -th propagation path
$\mathcal{P}_n^{(I_n)}, \mathbf{p}_n^{(k)}, \Gamma_n^{(k)}$	Set of interaction point coordinates along the n -th path, interaction point three-dimensional coordinate and interaction attenuation coefficient of the n -th path at the k -th interaction
M, m	Number of initialized rays, ray index
$\mathcal{P}_m^{(k)}, \prod_{l=1}^k \Gamma_m^{(l)}$	Set of interaction point coordinates, and cumulative product of the interaction attenuation coefficients up to the k -th interaction of the m -th ray
$\mathbf{d}_m^{(k)}, \alpha_m^{(k)}, \beta_m^{(k)}, \zeta_m^{(k)}$	Incident direction, incident angle, outgoing angle, and scatterer semantic class of the m -th ray at the k -th interaction
$\psi_m^{(k)}, \gamma_m^{(k)}$	Polarization angle, and angular deviation between the global and local coordinate systems of the m -th ray at the k -th interaction
$\mathcal{E}, \mathcal{D}_{tx,i}, \mathcal{D}_{rx,j}$	Environment, i -th Tx configuration, j -th Rx configuration, and the number of paths between the i -th Tx and j -th Rx
$\mathcal{A}_{tx,i}, \mathcal{A}_{rx,j}$	Antenna characteristics of the i -th Tx and the j -th Rx
$\mathbf{p}_{tx,i}, \mathbf{p}_{rx,j}$	Spatial coordinates of the i -th Tx and the j -th Rx
\mathcal{S}	Dataset

based radiance field representation, where dual multilayer perceptrons (MLPs) predict the attenuation and emission characteristics at each voxel. Note that NeRF² suffers from limited scalability due to dense real-world measurements. To alleviate this issue, NeWRF in [16] proposes a direction-aware training strategy that incorporates angle-of-arrival (AoA) priors into the learning process. This design not only reduces data requirements but also improves training efficiency. Building upon this direction, WRF-GS [17] further enhances computational efficiency and mitigates rendering latency by integrating 3D Gaussian splatting with neural modeling in the radio-frequency (RF) domain. While these methods enable efficient and accurate channel modeling, they still require substantial training data and exhibit limited generalization under environmental changes.

The third category of ICM is neural RT, which combines neural networks and the RT framework to implicitly model complex radio interactions within real-world environments and scenario geometries. By design rationale, neural RT-based approaches can achieve better generalization than the first two categories. They also have potentially higher modeling accuracy than conventional RT by the ability of learning from measured channel data rather than relying on simplified electromagnetic (EM) assumptions. An early work on neural RT is WiNeRT [18], which employs MLPs to simulate ray-surface interactions along propagation paths. Specifically, the neural network maps incident rays and surface properties to attenuated output signals at each interaction. To improve computational efficiency, SANDWICH [19] formulates ray trajectory generation as a sequential decision-making problem and proposes a training-efficient RT framework. Note that WiNeRT and SANDWICH considered a subset of propagation mechanisms only. The work in [20] introduces learnable wireless digital twins (LWDT), a more comprehensive framework that incorporates multiple propagation mechanisms. In LWDT, each propagation mechanism is modeled by a specialized neural module, and each interactive object is encoded by a dedicated neural network. While WiNeRT, SANDWICH and LWDT focus on indoor scenarios, the work in [21] proposes

a neural RT framework that can adapt to sparse training data and is validated using outdoor datasets.

Despite their advancements in modeling accuracy and efficiency, most existing neural RT methods [18]–[20] exhibit varying degrees of generalization capability. SANDWICH demonstrates reasonable generalization for unseen transmitter and receiver placements, but suffers from environmental dependence due to its autoregressive and reinforcement learning design. WiNeRT generalizes well to diverse indoor layouts, yet its reliance on absolute spatial information, such as normal vectors and input directions, results in significant spatial dependence. LWDT employs relative geometric features and object-level modeling, which improve its adaptability to unfamiliar indoor settings. However, when extended to outdoor environments, LWDT is constrained by sparse training data and tends to learn only local features of objects, which hinders comprehensive modeling of the overall EM behavior.

In this paper, we propose *Generalizable Neural RT* (GeNeRT), a physics-informed approach to ICM that has strong generalization, superior accuracy, and high efficiency. While inspired by WiNeRT's core architecture of using a dedicated outgoing ray prediction network for ray-surface interactions [18], GeNeRT distinguishes itself through innovations in the network architecture design and training strategy. The main features and novelties of our GeNeRT are summarized as follows:

First, GeNeRT achieves strong generalization by incorporating relative geometric features and scatterer semantics into the ray prediction network. This design reduces spatial dependency as incurred in [18] and hence enables reliable multipath component (MPC) prediction across both untrained regions within a scenario and entirely unseen environments. In addition, the incorporation of scatterer semantics, namely, the essential material features of scatterers that directly affect EM wave propagation behavior, enhances the representation of the intrinsic characteristics of the overall EM behavior.

Second, GeNeRT significantly improves the accuracy of ray-surface interaction modeling through a polarization-driven dual-branch network architecture for outgoing ray prediction.

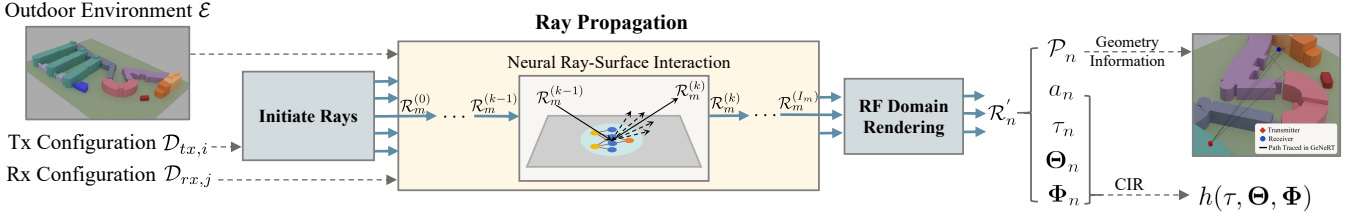


Fig. 1: Flowchart of GeNeRT.

Such dual-branch architecture explicitly models parallel and perpendicular polarization components according to the Fresnel reflection law. It thus effectively captures the polarization-dependent MPC properties. Additionally, we incorporate positional encoding (PosEnc) to process the angular information in the network input, as it enables the network to effectively capture complex nonlinear angular relationships. Furthermore, residual connections (ResNet) are integrated throughout the network to facilitate stable convergence and efficient training of deep structures.

Third, GeNeRT establishes an efficient two-stage training strategy that combines module-wise pre-training and system-wise end-to-end training. The module-wise pre-training phase uses polarization-specific datasets to guide the outgoing ray prediction network in capturing the universal polarization behavior. The system-wise end-to-end training phase learns site-specific EM propagation characteristics based solely on the receiver-side channel impulse responses (CIRs). This eliminates the dependence on full propagation path information, which was required in both WiNeRT and LWDT but hardly measurable in practice.

Extensive experiments validate the effectiveness of GeNeRT in outdoor scenarios. Specifically, GeNeRT consistently outperforms state-of-the-art neural RT baselines in the following aspects: 1) MPC prediction accuracy within the training region, 2) adaptability to varying meteorological factors, 3) intra-scenario spatial transferability, and 4) inter-scenario zero-shot generalization capability. Moreover, ablation experiments confirm the necessity of ResNet and the proposed two-stage training strategy. In addition, GeNeRT has reduced running time compared with Wireless Insite (WI). This is achieved by integrating GPU-tensorized ray-surface interaction and batched processing for multiple receivers.

The remainder of this paper is organized as follows. Section II introduces the overall framework of the proposed GeNeRT. Section III details the network architecture and training strategy of the learnable module within GeNeRT. Section IV presents the simulation results, and Section V concludes the paper. Key notations are listed in Table I.

II. OVERALL FRAMEWORK

This section first reviews the basic multipath channel model, then provides an overview of our GeNeRT framework, followed by a description of the neural ray-surface interaction.

A. Multipath Channel Model

When wireless signals traverse complex environments, they undergo diverse propagation mechanisms, such as free-space propagation, reflection, diffraction, and scattering, leading to

multiple paths. Each propagation path introduces amplitude attenuation and phase shifts, collectively shaping the composite signal. The multipath channel is typically represented by an omnidirectional CIR [22], expressed as

$$h(\tau, \Theta, \Phi) = \sum_n a_n \delta(\tau - \tau_n) \delta(\Theta - \Theta_n) \delta(\Phi - \Phi_n), \quad (1)$$

where τ_n , Θ_n , Φ_n and a_n denote the delay, the azimuth/elevation angle of departure (AoD), the azimuth/elevation AoA, and the total attenuation coefficient of the n -th path, respectively. Each a_n is determined by the total propagation distance d_n , the number of interactions I_n , and the attenuation coefficient at each interaction $\Gamma_n^{(k)}$, for $k = 1, 2, \dots, I_n$. It can be expressed as

$$a_n = \underbrace{\frac{\lambda}{4\pi d_n}}_{\text{1st}} \cdot \underbrace{\left(\prod_{k=1}^{I_n} \Gamma_n^{(k)} \right)}_{\text{2nd}} \cdot \underbrace{e^{-j\frac{2\pi}{\lambda} d_n}}_{\text{3rd}}, \quad (2)$$

which incorporates three key components: the first term is the free-space attenuation coefficient magnitude, the second term is the attenuation coefficient due to the interaction of the ray with the environment, and the third one represents the phase change caused by free-space propagation. Therefore, multipath channel modeling can be reformulated as the task of predicting a set of MPCs, each characterized by a set

$$\mathcal{H}_n = \{\tau_n, \Theta_n, \Phi_n, a_n\}, \quad (3)$$

where a_n depends on d_n , I_n , and $\left\{ \Gamma_n^{(k)} \right\}_{k=1}^{I_n}$.

B. Overview of GeNeRT Framework

The core idea of GeNeRT lies in replacing the mathematical equations used to model ray-surface interactions in conventional RT with a neural network representation. As illustrated in Fig. 1, rays are emitted from the transmitter (Tx) and propagate through the environment via successive interactions with environmental scatterer surfaces. Each ray is eventually either terminated or received. After collecting all rays that successfully reach the receiver (Rx), GeNeRT generates the CIR for the corresponding Tx-Rx pair and provides the geometric information of propagation paths. To be more specific, GeNeRT can be represented by a forward function GeNeRT_θ , which is formulated as

$$\text{GeNeRT}_\theta : (\mathcal{E}, \mathcal{D}_{tx,i}, \mathcal{D}_{rx,j}) \mapsto \left(h(\tau, \Theta, \Phi), \left\{ \mathcal{P}_n^{(I_n)} \right\}_{n=1}^{N_{i,j}} \right). \quad (4)$$

The input to this function consists of propagation environment and Tx/Rx configurations. Concretely, the propagation environment is defined as \mathcal{E} , which consists of a series of convex

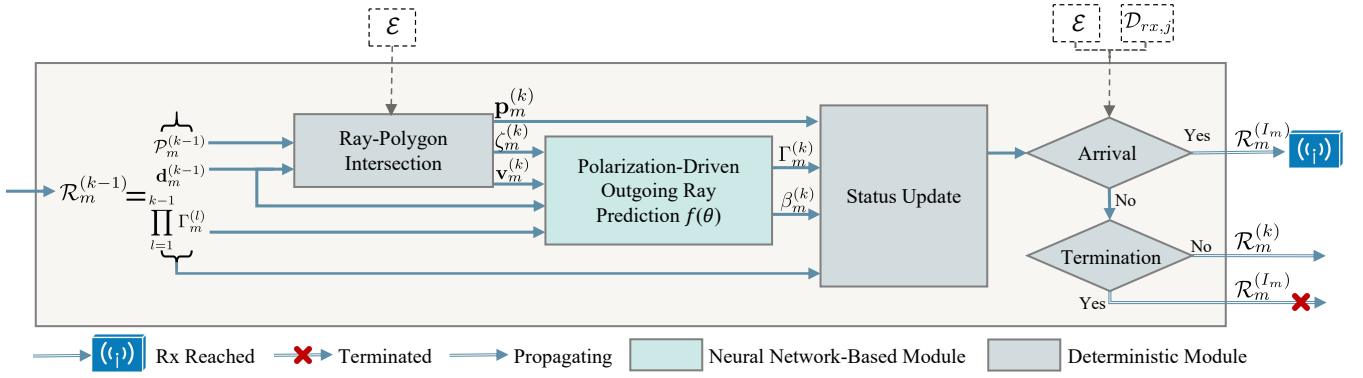


Fig. 2: Flowchart of Neural Ray-Surface Interaction.

polygonal surfaces sharing the same number of vertices. Each surface is associated with a one-hot encoded scatterer semantic class, denoted as ζ . Here, the scatterer semantics refer to the essential material features of scatterers that directly affect EM wave propagation behavior, and the scatterer semantic class can be extracted from the physical environment via texture recognition techniques or other appropriate approaches. The configurations of the i -th Tx and j -th Rx, denoted by $\mathcal{D}_{tx,i}$ and $\mathcal{D}_{rx,j}$, respectively, are defined as

$$\mathcal{D}_{tx,i} = \{\mathcal{A}_{tx,i}, \mathbf{p}_{tx,i}\}, \mathcal{D}_{rx,j} = \{\mathcal{A}_{rx,j}, \mathbf{p}_{rx,j}\}, \quad (5)$$

where $\mathcal{A}_{tx,i}$ ($\mathcal{A}_{rx,j}$) denotes the antenna characteristics of the Tx (Rx), including the radiation pattern and polarization of the antennas; $\mathbf{p}_{tx,i}$ ($\mathbf{p}_{rx,j}$) represents the spatial coordinates of the Tx (Rx), respectively. Based on these inputs, the GeNeRT $_{\theta}$ in (4) then maps them to $h(\tau, \Theta, \Phi)$ in (1) and $\{\mathcal{P}_n^{(I_n)}\}_{n=1}^{N_{i,j}}$, where $N_{i,j}$ denotes the number of propagation paths between the i -th Tx and the j -th Rx, I_n represents the total number of ray-surface interactions along the n -th path, $\mathcal{P}_n^{(I_n)} = \{\mathbf{p}_n^{(k)}\}_{k=1}^{I_n}$ stores all interaction points along this path, where $\mathbf{p}_n^{(k)}$ denotes the 3D coordinate at the k -th interaction of the n -th path.

The implementation process of GeNeRT comprises the following three steps.

1) *Ray Initialization*: We launch M different rays from the Tx, each initialized with a state $\mathcal{R}_m^{(0)}$, as defined later. Please be reminded that a “ray” is any simulated propagation trajectory launched from the Tx, whereas a “path” is a ray that successfully reaches the Rx to contribute to the channel response.

2) *Ray Propagation*: After initialization, rays propagate through the environment and interact with scatterer surfaces. During this process, GeNeRT tracks each ray’s propagation using a ray state. For each ray m , the corresponding state at the k -th interaction with the environment is defined as

$$\mathcal{R}_m^{(k)} = \left\{ \mathcal{P}_m^{(k)}, \mathbf{d}_m^{(k)}, \prod_{l=1}^k \Gamma_m^{(l)} \right\}, \quad (6)$$

where the maximum value of k is defined as I_m and has two distinct meanings. For rays that successfully reach the Rx, it is defined as the total number of interactions experienced before arrival. For terminated rays, it represents the number

of interactions completed prior to termination. The tuple $\mathcal{P}_m^{(k)}$ stores the spatial coordinates of all interaction points up to the k -th interaction, and is initialized as an empty tuple when $k = 0$. The unit direction vector $\mathbf{d}_m^{(k)}$ represents the propagation direction of the m -th ray after the k -th interaction, with $\mathbf{d}_m^{(0)}$ denoting the initial direction. The third term corresponds to the cumulative product of the ray’s interaction coefficients up to the k -th interaction, initialized to 1 when $k = 0$.

The state in (6) is iteratively updated as the ray propagates and interacts with the environment. Specifically, a neural network-based module is employed to predict interaction coefficients and outgoing directions, while geometric calculations and ray state updates are handled through deterministic procedures. Further details are provided in Section II-C.

3) *RF Domain Rendering*: In general, rendering is the process of transforming abstract data into a form that enables analysis, comprehension, and visualization. In the RF domain, rendering is the process to compute the desired characteristics of RF signals [21]. To be more specific, taking the n -th propagation path as an example, this step serves as the post-processing of the information in $\mathcal{R}_n^{(I_n)}$. On one hand, we preserve the original interaction point coordinates in $\mathcal{P}_n^{(I_n)}$; on the other hand, we extract the characteristics \mathcal{H}_n in (3), where the parameters τ_n, Θ_n, Φ_n are determined by the interaction points $\mathcal{P}_n^{(I_n)}$ along with the positions of the Tx and Rx, while a_n can be readily obtained from (2). In summary, the output of this step is denoted as $\mathcal{R}_n' = \{\mathcal{P}_n^{(I_n)}, \mathcal{H}_n\}$.

C. Neural Ray-Surface Interaction

This subsection discusses the detailed implementation process of the ray-surface interaction step, with its flowchart illustrated in Fig. 2. The ray-surface interaction may in principle involve multiple propagation mechanisms, such as reflection, refraction, scattering, and diffraction. To maintain a clear focus, this work is concentrated on reflection, which we consider foundational to the modeling of other propagation mechanisms. The overall procedure consists of the following four steps.

1) *Ray-Polygon Intersection*: We model the scatterer surfaces via polygonal primitives (e.g., triangle) with an identical number of vertices. Specifically, considering the k -th interac-

tion of the m -th ray as an example, the corresponding ray equation is formulated as

$$\mathbf{p}(x) = \mathbf{p}_m^{(k-1)} + x \cdot \mathbf{d}_m^{(k-1)}, \quad (7)$$

where $\mathbf{p}(x) \in \mathbb{R}^{3 \times 1}$ is the coordinate of any point on the ray, and x is the distance from the point to the starting point. Initially, we solve this equation in conjunction with the plane equations of all surfaces in the environment to compute potential intersection points between the ray and these planes. Subsequently, the Möller–Trumbore algorithm [23] is applied to verify whether these intersection points are contained within their corresponding surfaces. Points satisfying this condition are classified as candidate intersection points. Ultimately, the closest candidate point to the ray origin is selected as $\mathbf{p}_m^{(k)}$, representing the spatial coordinates of the k -th interaction along the m -th ray. Once $\mathbf{p}_m^{(k)}$ is determined, the corresponding polygonal surface is retrieved, from which the scatterer semantic class $\zeta_m^{(k)}$ (expressed as a one-hot vector) and the surface normal vector $\mathbf{v}_m^{(k)}$ are obtained. Notably, this step is computation-intensive. To improve its runtime efficiency, we adopt a GPU-accelerated vectorized Möller–Trumbore algorithm, an efficient nearest-intersection filtering strategy, and a fully tensorized computation pipeline executed on GPU.

2) *Polarization-Driven Outgoing Ray Prediction:* In the previous step, we have identified the interaction positions along with their corresponding properties, including the scatterer semantic class and surface normal vector. The current step aims to predict the outgoing direction $\mathbf{d}_m^{(k)}$ and the interaction coefficient $\Gamma_m^{(k)}$. While conventional RT frameworks (e.g., Sionna RT [24]) explicitly model this process using the law of reflection and Fresnel equations, our framework employs a neural network to implicitly learn the underlying physical principles to achieve a more accurate and efficient MPC prediction.

In the reflection field, the reflected angle $\beta_m^{(k)}$ and interaction coefficient $\Gamma_m^{(k)}$ depend on the incident direction, surface normal, polarization angle, and scatterer semantic class. To reduce spatial dependency and enhance the generalization capability, the network input is designed using relative geometric features instead of absolute coordinates and directions. Specifically, the incident angle $\alpha_m^{(k)}$ is computed from $\mathbf{d}_m^{(k-1)}$ and $\mathbf{v}_m^{(k)}$, while the angular offset $\gamma_m^{(k)}$ is derived from the polarization angle $\psi_m^{(k)}$, which quantifies the deviation between the electric field oscillation direction $\hat{\mathbf{e}}_E$ and the plane of incidence:

$$\psi_m^{(k)} = \arccos \left(\frac{\mathbf{v}_m^{(k)} \times \mathbf{d}_m^{(k-1)}}{\|\mathbf{v}_m^{(k)} \times \mathbf{d}_m^{(k-1)}\|} \cdot \hat{\mathbf{e}}_E \right). \quad (8)$$

This angle plays a crucial role in determining interaction loss, primarily influenced by two factors. The first is the angular deviation between the global and local coordinate systems, corresponding to $\gamma_m^{(k)}$, which can be computed by assuming $\hat{\mathbf{e}}_E$ is vertically upward in (8). The second is the orientation of $\hat{\mathbf{e}}_E$, which depends on the ray's historical interactions and is difficult to model explicitly. To approximate this effect, we use the cumulative product of the previous interaction

coefficients, denoted as $\prod_{l=1}^{k-1} \Gamma_m^{(l)}$. This design allows the network to accurately capture the polarization-related behaviors. Accordingly, the polarization-driven outgoing ray prediction network is defined as:

$$f : (\alpha_m^{(k)}, \zeta_m^{(k)}, \gamma_m^{(k)}, \prod_{l=1}^{k-1} \Gamma_m^{(l)}; \theta) \mapsto (\beta_m^{(k)}, \Gamma_m^{(k)}), \quad (9)$$

where θ denotes the trainable parameters.

3) *Status Update:* At each ray-surface interaction, the state is updated to reflect new propagation conditions. Specifically, for the k -th interaction along the m -th ray, the predicted reflection field yields the reflected angle $\beta_m^{(k)}$ and interaction coefficient $\Gamma_m^{(k)}$, which are used to update the ray state. The updated state $\mathcal{R}_m^{(k)}$, derived from the previous state $\mathcal{R}_m^{(k-1)}$, can be expressed as

$$\begin{aligned} \mathcal{R}_m^{(k)} &= \text{Update}(\mathcal{R}_m^{(k-1)}) \\ &= \{\mathcal{P}_m^{(k-1)} \oplus \mathbf{p}_m^{(k)}, \mathbf{d}_m^{(k)}, \Gamma_m^{(k)} \cdot \prod_{l=1}^{k-1} \Gamma_m^{(l)}\}, \end{aligned} \quad (10)$$

where \oplus denotes the tuple concatenation operation, and the outgoing direction $\mathbf{d}_m^{(k)}$ can be calculated by

$$\begin{aligned} \mathbf{d}_m^{(k)} &= \cos \beta_m^{(k)} \cdot \mathbf{v}_m^{(k)} \\ &+ \sin \beta_m^{(k)} \cdot \frac{\mathbf{d}_m^{(k-1)} - (\mathbf{d}_m^{(k-1)} \cdot \mathbf{v}_m^{(k)}) \mathbf{v}_m^{(k)}}{\|\mathbf{d}_m^{(k-1)} - (\mathbf{d}_m^{(k-1)} \cdot \mathbf{v}_m^{(k)}) \mathbf{v}_m^{(k)}\|}. \end{aligned} \quad (11)$$

4) *Arrival/Termination Judgment:* Following the computation of the outgoing rays and their associated states, each ray undergoes a sequential evaluation to determine whether it (i) reaches a Rx, (ii) continues to propagate with an updated state, or (iii) terminates because of environmental boundaries, a predefined maximum number of interactions, or a predefined power threshold.

III. POLARIZATION-DRIVEN OUTGOING RAY PREDICTION

The core component of GeNeRT is the outgoing ray prediction network $f(\theta)$, which plays a critical role in accurately predicting MPCs and interaction characteristics. This section begins with an introduction to the Fresnel reflection law, then describes the network architecture of $f(\theta)$, and concludes with the training strategy employed for the network.

A. Fresnel Reflection Law

The Fresnel reflection law rigorously defines the reflection attenuation coefficient, which characterizes the signal strength and field distribution of the reflected wave and is directly related to the accuracy of reflected field prediction. For simplicity, the reflection coefficient $\Gamma_n^{(k)}$ is denoted as Γ^r in the following derivations. It is defined as

$$\Gamma^r = \frac{\mathbf{E}^r}{\mathbf{E}^i}, \quad (12)$$

where \mathbf{E}^r and \mathbf{E}^i represent the reflected and incident electric field intensities, respectively. However, directly modeling the electric field in 3D space is inherently complex, requiring its decomposition into components perpendicular and parallel to

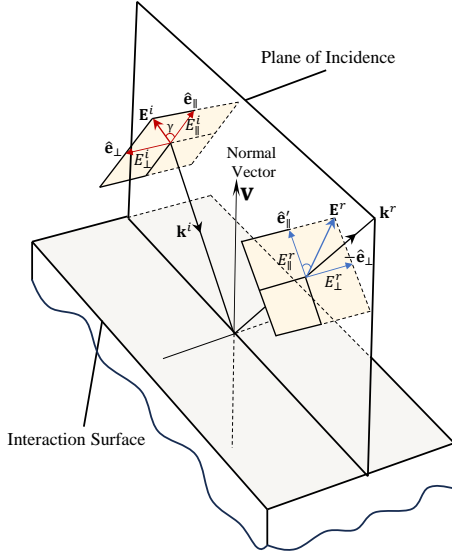


Fig. 3: Schematic diagram of the decomposition of the incident and reflected waves in parallel and perpendicular polarization direction. \mathbf{k}^i and \mathbf{k}^r represent the propagation directions of the incident and reflected waves, respectively.

the plane of incidence [25]. Fig. 3 illustrates the decomposition details of the EM wave before and after reflection. The incident electric field \mathbf{E}^i can be decomposed as

$$\mathbf{E}^i = E_{\perp}^i \cdot \hat{\mathbf{e}}_{\perp} + E_{\parallel}^i \cdot \hat{\mathbf{e}}_{\parallel}, \quad (13)$$

where $\hat{\mathbf{e}}_{\perp}$ and $\hat{\mathbf{e}}_{\parallel}$ denote the unit vectors in the directions perpendicular and parallel to the plane of incidence, respectively. Given the polarization angle ψ , the perpendicular and parallel components of the incident electric field, E_{\perp}^i and E_{\parallel}^i , can be computed as

$$E_{\perp}^i = |\mathbf{E}^i| \cdot \sin(\psi), \quad E_{\parallel}^i = |\mathbf{E}^i| \cdot \cos(\psi). \quad (14)$$

Similarly, the reflected electric field can also be expressed as

$$\mathbf{E}^r = E_{\perp}^r \cdot \hat{\mathbf{e}}_{\perp} + E_{\parallel}^r \cdot \hat{\mathbf{e}}'_{\parallel}, \quad (15)$$

where $\hat{\mathbf{e}}'_{\parallel}$ represents the unit vector in the direction parallel to the plane of incidence for the reflected wave. According to reference [25], the relationship between the reflected and incident field components is given by

$$\begin{bmatrix} E_{\perp}^r \\ E_{\parallel}^r \end{bmatrix} = \begin{bmatrix} \Gamma_{\perp} & 0 \\ 0 & \Gamma_{\parallel} \end{bmatrix} \cdot \begin{bmatrix} \sin(\psi) \\ \cos(\psi) \end{bmatrix} \cdot |\mathbf{E}^i|, \quad (16)$$

where Γ_{\perp} and Γ_{\parallel} are the parallel and perpendicular polarization component of reflection coefficient Γ^r , respectively. These components depend solely on the angle of incidence and the material properties [25].

In summary, the reflection coefficient Γ^r is obtained in two stages: first, computing each polarization component based on material properties and incident angle; second, weighting them by the sine and cosine of the polarization angle ψ .

B. Network Architecture

The architecture of the proposed outgoing ray prediction network $f(\theta)$ is illustrated in Fig. 4. It consists of three

functionally coordinated modules: the outgoing angle prediction module, the polarization component prediction module, and the polarization fusion module, each designed to capture distinct but complementary aspects of EM ray-surface interactions.

The network first takes as input the incident angle $\alpha_m^{(k)}$ and the scatterer semantic class $\zeta_m^{(k)}$. The former is encoded using the PosEnc defined in (17), where L denotes the encoding dimension controlling the frequency granularity. The latter is embedded into a continuous latent vector via an embedding layer. These two encoded inputs are concatenated and transformed by a latent space expansion MLP to form a unified feature vector. This feature is then processed by two parallel branches. The outgoing angle prediction module estimates $\beta_m^{(k)}$ using a stack of feed-forward network (FFN) blocks with ResNet. In parallel, the polarization component prediction module employs a Fresnel-inspired dual-branch architecture to separately compute the parallel $\Gamma_{\parallel,m}^{(k)}$ and perpendicular $\Gamma_{\perp,m}^{(k)}$ components of $\Gamma_m^{(k)}$, each through its own FFN-based pathway and dedicated output layer. Finally, the predicted polarization components, along with the cumulative coefficient $\sum_{l=1}^{k-1} \Gamma_m^{(l)}$ and the angular offset $\gamma_m^{(k)}$ (encoded via PosEnc), are concatenated and passed to the polarization fusion module, which refines the combined input through stacked FFN blocks and outputs the final interaction coefficient $\Gamma_m^{(k)}$.

C. Training Strategy

The training procedure of the network $f(\theta)$ consists of two phases: modular-wise pre-training and system-wise end-to-end training. Before elaborating on these training phases, we first introduce the dataset with polarization components.

When EM waves interact with the environment, they typically contain both parallel and perpendicular polarization components simultaneously. Directly using such data for training introduces two challenges: first, it demands highly precise polarization angles; second, the underlying patterns the network needs to capture become overly complex. Therefore, it is crucial to construct datasets containing only a single polarization component (either parallel or perpendicular) for initial training, enabling the network to effectively learn characteristics of each polarization component. We denote the dataset with parallel and perpendicular polarization components as \mathcal{S}_{\parallel} and \mathcal{S}_{\perp} . To precisely control the target link to contain exclusively perpendicular or parallel polarization components, we select only single-reflection paths and employ specialized configurations of Tx and Rx. To be more precise, by employing a particular Tx polarization mode and carefully arranging the positions of Tx and Rx, we ensure that the polarization angle ψ of the incident EM waves on single-reflection paths is either 0 or $\pi/2$. Specifically, paths with a polarization angle of 0 are leveraged to construct dataset \mathcal{S}_{\parallel} , while those with a polarization angle of $\pi/2$ are utilized to form dataset \mathcal{S}_{\perp} . The explicit formulations of \mathcal{S}_{\parallel} and \mathcal{S}_{\perp} are given as

$$\mathcal{S}_{\lambda} = \{(\mathbf{x}_n, \mathbf{y}_{\lambda,n})\}_{n=1}^{N_{\text{samples}}}, \quad (18)$$

where N_{samples} denotes the number of samples, and $\lambda \in \{\perp, \parallel\}$. The input \mathbf{x}_n and corresponding label $\mathbf{y}_{\lambda,n}$ are explicitly

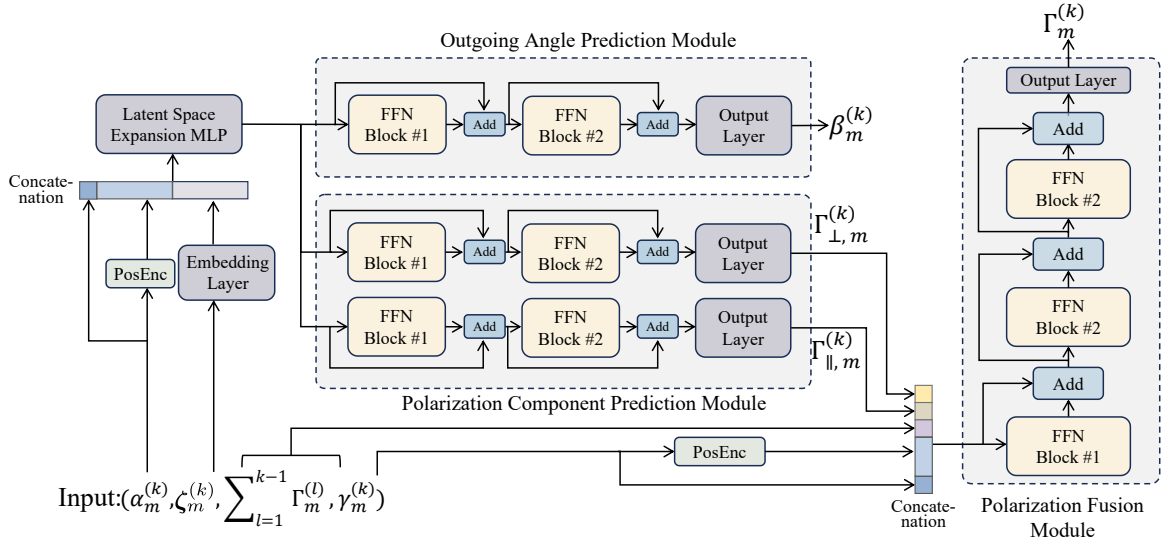


Fig. 4: Network architecture for the proposed polarization-driven outgoing ray prediction network $f(\theta)$.

defined as

$$\mathbf{x}_n = [\zeta_n^{(1)}, \alpha_n^{(1)}], \quad \mathbf{y}_{\lambda,n} = [\beta_n^{(1)}, \Gamma_{\lambda,n}^{(1)}], \quad (19)$$

where $\zeta_n^{(1)}$, $\alpha_n^{(1)}$, $\beta_n^{(1)}$ and $\Gamma_{\lambda,n}^{(1)}$ are the scatterer semantic class (one-hot encoding), incident angle, outgoing angle and polarization-specific component of attenuation coefficient for each single-reflection path.

During the module-wise pre-training phase, we leverage \mathcal{S}_{\parallel} and \mathcal{S}_{\perp} to train the embedding layer, latent space expansion MLP, polarization component prediction module, and outgoing angle prediction module. Specifically, we adopt a greedy layer-wise training strategy. First, the $\Gamma_{\parallel,n}^{(1)}$ in \mathcal{S}_{\parallel} was used to train the embedding layer, the latent space expansion MLP, and the lower branch of polarization component prediction module. Next, we froze their weights and use the $\Gamma_{\perp,n}^{(1)}$ in \mathcal{S}_{\perp} to train the upper branch of the polarization component prediction module. Finally, we freeze the parameters of all previously trained modules and use the label $\beta_n^{(1)}$ from \mathcal{S}_{\parallel} and \mathcal{S}_{\perp} to train the outgoing angle prediction module. Furthermore, when predicting the polarization components of $\Gamma_m^{(k)}$, we employ normalized mean square error (NMSE) as the loss function; when predicting the outgoing angle, we represent the angle as a tuple of (sin, cos) and leverage mean square error (MSE) as the loss function:

$$\text{MSE} = (\sin \hat{\beta} - \sin \beta)^2 + (\cos \hat{\beta} - \cos \beta)^2, \quad (20)$$

where $\hat{\beta}$ is the predicted outgoing angle.

During the system-wise end-to-end training phase, we use the CIR of each Tx-Rx pair to further train $f(\theta)$. At this point, the configurations of Tx and Rx are no longer meticulously arranged; instead, they are adjusted based on practical requirements, and the propagation paths may involve multiple interactions. The dataset at this stage can be written as

$$\mathcal{S} = \{(\mathcal{X}_{i,j}, \mathcal{Y}_{i,j}) \mid i = 1, \dots, N_t, j = 1, \dots, N_r\}, \quad (21)$$

where N_t and N_r are the numbers of the Tx and Rx, respectively. The input $\mathcal{X}_{i,j}$ and corresponding label $\mathcal{Y}_{i,j}$ are defined as

$$\mathcal{X}_{i,j} = \{\mathcal{E}, \mathcal{D}_{tx,i}, \mathcal{D}_{rx,j}\}, \quad \mathcal{Y}_{i,j} = \{\mathcal{H}_n\}_{n=1}^{N_{i,j}}, \quad (22)$$

where $N_{i,j}$ denotes the number of propagation paths between the i -th Tx and the j -th Rx. Prior to training the network, we utilize the time delay τ_n and AoA Φ_n in \mathcal{H}_n to establish a bijection ϕ between the predicted set $\hat{\mathcal{Y}}_{i,j}$ and the label set $\mathcal{Y}_{i,j}$. The predicted set are defined as

$$\hat{\mathcal{Y}}_{i,j} = \{\hat{\mathcal{H}}_n\}_{n=1}^{\hat{N}_{i,j}}, \quad (23)$$

where $\hat{N}_{i,j}$ is the predicted number of paths between the i -th Tx and the j -th Rx. To be more specific, bijection ϕ is determined as

$$\min_{\phi: \hat{\mathcal{Y}}_{i,j} \rightarrow \mathcal{Y}_{i,j}} \sum_{\hat{\mathcal{H}}_n \in \hat{\mathcal{Y}}_{i,j}} \mathcal{L}_{\text{geo}}(\hat{\mathcal{H}}_n, \phi(\hat{\mathcal{H}}_n)), \quad (24)$$

where $\mathcal{L}_{\text{geo}}(\hat{\mathcal{H}}, \phi(\hat{\mathcal{H}}))$ measures the temporal and spatial discrepancy between the sets, and is defined as

$$\mathcal{L}_{\text{geo}}(\hat{\mathcal{H}}, \phi(\hat{\mathcal{H}})) = \sum_{x \in \{\tau_n, \Phi_n\}} \frac{\|\hat{x} - x\|_2^2}{\|x\|_2^2}. \quad (25)$$

Afterward, we use the bijection ϕ to assign label values to the predicted attenuation coefficients and take their NMSE as the loss function during training. During this phase, we focus on optimizing specific modules of the network. Unless otherwise specified, only the weights of the polarization fusion module are activated during training.

IV. EXPERIMENT RESULTS

In this section, we evaluate the proposed GeNeRT framework through comprehensive experiments. Section IV-A introduces the data generation process and scenario setup, while

$$\text{PosEnc}(x) = [\sin(2^1 x), \cos(2^1 x), \dots, \sin(2^L x), \cos(2^L x)]^T, \quad x \in (0, \frac{\pi}{2}) \quad (17)$$

TABLE II: Overview of constructed datasets.

	Dataset	Scenario	Humidity Level	Horizontal Positions of Rxs	Rx Height	Rx Count	Train/Val/Test Ratio
Module-Wise Pre-Training	S_{\perp}	Scenario 1	Dry	Polygon Layout 1 in Fig. 5(b)	2 m	13500	80 / 20 / 0
	S_{\parallel}	Scenario 1	Dry	Polygon Layout 1 in Fig. 5(b)	2 m	13500	80 / 20 / 0
System-Wise End-to-End Training	S_1	Scenario 2	Dry	Polygon Layout 2 in Fig. 5(d)	6 m	2029	80 / 10 / 10
	S_2	Scenario 2	Medium Dry	Polygon Layout 2 in Fig. 5(d)	6 m	2029	80 / 10 / 10
	S_3	Scenario 2	Wet	Polygon Layout 2 in Fig. 5(d)	6 m	2029	80 / 10 / 10
Generalization Test	S_4	Scenario 2	Dry	Polygon Layout 3 in Fig. 5(d)	6 m	2520	0 / 0 / 100
	S_5	Scenario 2	Dry	Route Layout 1 in Fig. 5(d)	6 m	1431	0 / 0 / 100
	$S_6 - S_{14}$	Scenario 2	Dry	Polygon Layout 2 in Fig. 5(d)	varied*	2029	0 / 0 / 100
	S_{15}	Scenario 3	Dry	Polygon Layout 4 in Fig. 5(f)	6 m	2352	0 / 0 / 100

* Rx heights for S_6 to S_{14} are set to 2 m, 4 m, 8 m, 10 m, 12 m, 14 m, 16 m, 18 m, and 20 m, respectively.

Section IV-B details the dataset construction. The network architecture and training details are presented in Section IV-C. Section IV-D presents ablation experiments on key components of the network. Adaptability to environmental humidity is evaluated in Section IV-E, followed by generalization tests in Section IV-F. Finally, Section IV-G compares the simulation time of GeNeRT with the conventional RT.

A. Data Collection

In this paper, we leverage WI to generate labeled data. WI is a commonly used RT software that can generate CIRs. It can trace the rays propagating in the environment and yield the corresponding channel characteristics.

1) *Scenario Setup*: We consider the following three real-world outdoor scenarios for data generation:

- **Scenario 1: Rosslyn.** This scenario, depicted in Figs. 5(a) and (b), represents a section of Rosslyn, Virginia, and is publicly available in WI as an urban scenario. It occupies a region measuring $150 \text{ m} \times 160 \text{ m} \times 80 \text{ m}$ (width \times length \times height), containing 10 buildings and 60 surfaces, each with sides perpendicular to the ground.
- **Scenario 2: SJTU-SEIEE.** This scenario, as depicted in Figs. 5(c) and Fig 5(d), is the School of Electronic Information and Electrical Engineering at Shanghai Jiao Tong University on the Minhang campus. It is reconstructed using an oblique photogrammetry-based monolithic modeling technique¹. It spans a $195 \text{ m} \times 255 \text{ m} \times 30 \text{ m}$ region and features a dragon-shaped layout consisting of 3 buildings and 1606 surfaces.
- **Scenario 3: SJTU-ME.** This scenario is the School of Mechanical Engineering at Shanghai Jiao Tong University on the Minhang campus, as shown in Fig. 5(e) and Fig. 5(f). This scenario is also reconstructed by the oblique photogrammetry-based monolithic modeling technique. It covers a region measuring $195 \text{ m} \times 255 \text{ m} \times 30 \text{ m}$, comprising 6 buildings and 522 surfaces.

In these scenarios, each scatterer semantic class is associated with a specific material type for simplicity², defined according to the ITU-R standard [26] and illustrated in different colors in Figs. 5(a), (c), and (e). Additionally, three humidity levels

¹This technology is primarily based on multi-angle aerial imagery to obtain high-precision mesh models, after which it employs deep learning and segmentation algorithms to automatically identify individual buildings or structures.

²Note that scatterer semantics contain more aspects than material type, but mainly material type is considered in this work as an initial trial.

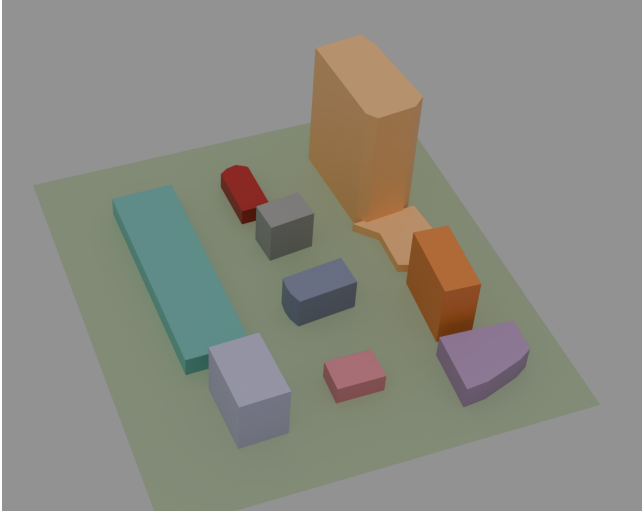
are considered, with the corresponding material parameters set as follows:

- **Dry:** The conductivity and relative permittivity of all materials are set according to the specifications in [26], where the ground is configured as Very Dry Ground.
- **Medium Dry:** The ground is set as Medium Dry Ground, while the conductivity and relative permittivity of all other materials are increased by 30% compared to the dry condition.
- **Wet:** The ground is set as Wet Ground, while the conductivity and relative permittivity of all other materials are increased by 60% compared to the dry condition.

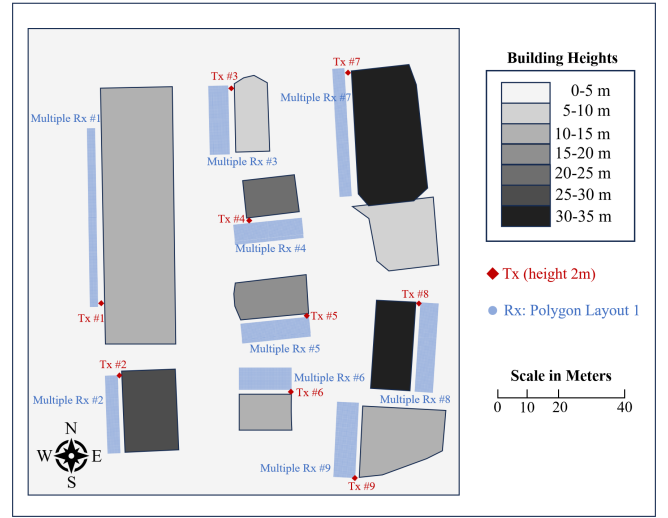
2) *Data Description*: Based on the three scenarios described above, we construct three types of datasets to support different stages of training and evaluation: module-wise pre-training, system-wise end-to-end training, and generalization test. All datasets are generated under a consistent RT configuration unless otherwise specified. In particular, rays are launched uniformly at 0.4° intervals, and both the Tx and Rx are equipped with isotropic antenna³ with a gain of 0 dBi. The transmission power is set to 0 dBm, and the carrier frequency is 3.5 GHz. An overview of the constructed datasets is given in Table II, with construction details presented below:

- **Module-wise pre-training:** To isolate specific polarization components, we construct S_{\parallel} and S_{\perp} from Scenario 1 using single-reflection paths. Tx and Rx are placed at the same height (2 m) and located near building edges. S_{\parallel} includes horizontally polarized signals reflected by buildings and vertically polarized signals reflected by the ground, while S_{\perp} consists of the opposite combinations.
- **System-wise end-to-end training:** The datasets S_1 - S_3 constructed from Scenario 2 differ exclusively in the humidity levels. At this stage, we collect the CIR for each Tx-Rx pair as defined in (22).
- **Generalization test:** To evaluate the model's generalization performance, we construct twelve challenging datasets covering two aspects: intra-scenario spatial transferability and inter-scenario zero-shot generalization capability. Datasets S_4 - S_{14} from Scenario 2 are constructed for the former. Specifically, S_4 and S_5 vary the horizontal positions of the Rxs while keeping their height fixed, whereas S_6 - S_{14} vary the Rx heights at fixed horizontal

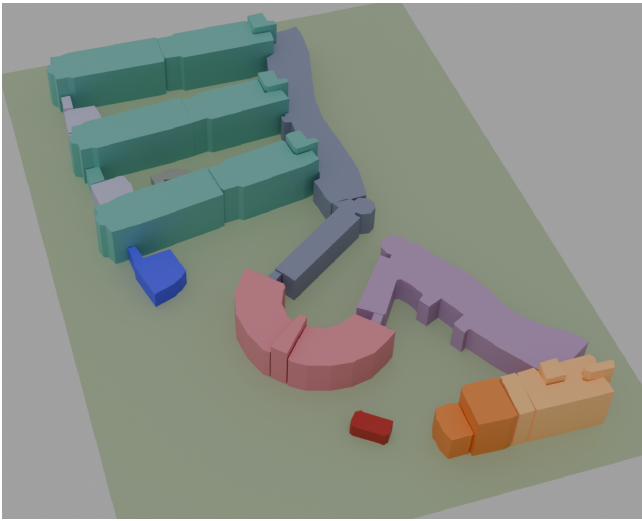
³Note that the proposed approach is applicable to arbitrary antenna patterns by incorporating the corresponding antenna gain on each ray.



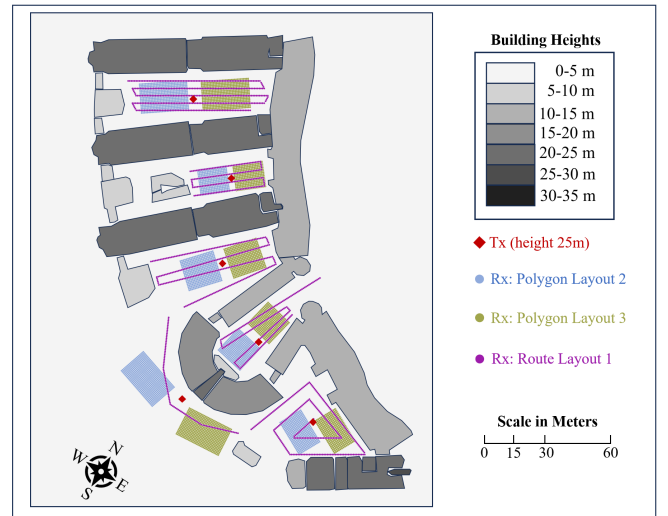
(a) Aerial view of the buildings in Scenario 1.



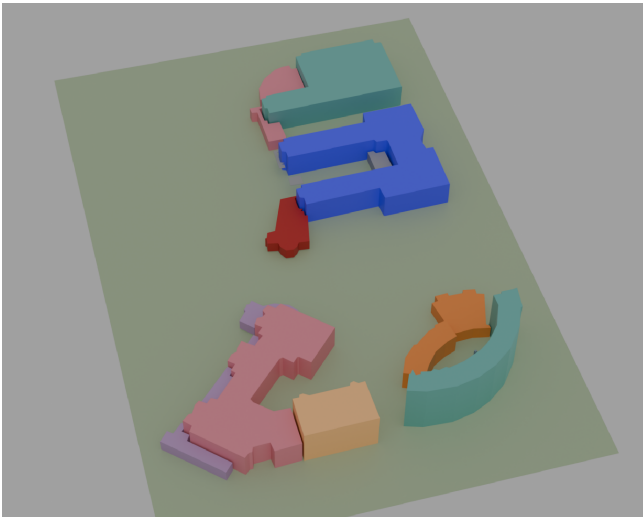
(b) Bird's eye view of Scenario 1 and the horizontal positions of Tx's and Rx's.



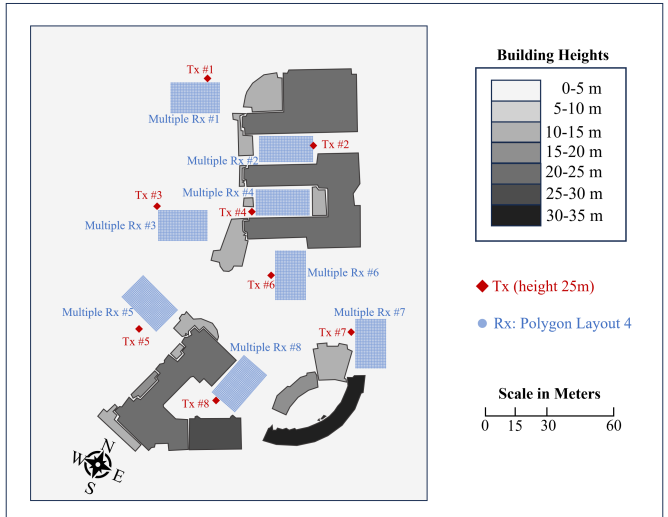
(c) Aerial view of the buildings in Scenario 2.



(d) Bird's eye view of Scenario 2 and the horizontal positions of Tx's and Rx's.



(e) Aerial view of the buildings in Scenario 3.



(f) Bird's eye view of Scenario 3 and the horizontal positions of Tx's and Rx's.

Fig. 5: Scenarios used to construct the dataset and the distribution of Tx's and Rx's within these scenarios.

positions, as illustrated in Fig. 6. Dataset \mathcal{S}_{15} from Scenario 3 is constructed for the latter, where the original scenario is replaced with Scenario 3 to test cross-scenario generalization. Additionally, at this stage, we also collect the CIR for each Tx–Rx pair as defined in (22).

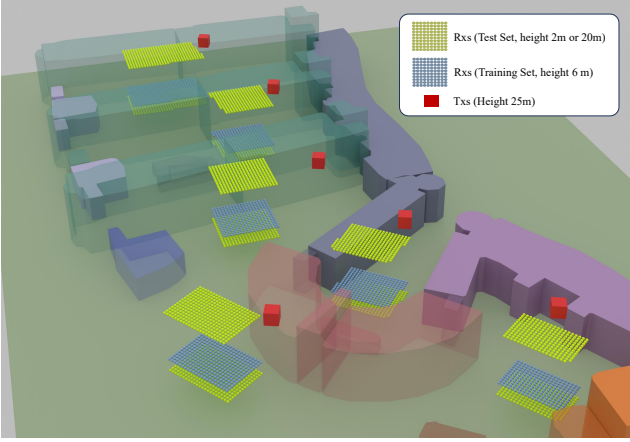


Fig. 6: Distribution of Txs and Rxs in datasets \mathcal{S}_6 to \mathcal{S}_{14} . For clarity, only the lowest and highest Rxs are shown; the remaining Rxs are positioned at intermediate heights of 4 m and from 8 m to 20 m in 2 m increments. Certain buildings are intentionally blurred to emphasize Rxs’ spatial locations.

B. Simulation Setup

1) *Network Architecture and Hyperparameters:* The network architecture introduced in Section III is specified in detail as follows. The output dimension of the embedding layer is set to 5, which is then expanded by a latent space MLP containing a single hidden layer with 32 neurons. The first FFN block consists of input and output layers with 64 neurons and a hidden layer with 32 neurons, while the second block comprises 32 neurons for both input and output, and a hidden layer with 16 neurons. The encoding dimension L in the PosEnc is set to 4. ReLU is used as the nonlinear activation function throughout the network. To train this network, we adopt the Adam optimizer with a batch size of 64. For module-wise pre-training, the model is trained for 400 epochs with an initial learning rate of $1e^{-3}$, which is halved every 80 epochs. For system-wise end-to-end training, we use 200 training epochs, with an initial learning rate of $4e^{-4}$, reduced by half every 50 epochs. Weight parameters are initialized using the Xavier Uniform method.

2) *Evaluation Metrics:* After obtaining the ground truth (GT) label \mathcal{H}_n for each predicted $\hat{\mathcal{H}}_n$ via the mapping defined in (24), we assess the MPC prediction performance using the following three metrics:

- **Overall prediction error (Overall Error):** This metric quantifies the overall modeling error across all propagation paths and channel elements. For each propagation path, we compute the sum of element-wise NMSEs between $\hat{\mathcal{H}}_n$ and \mathcal{H}_n , followed by averaging across all paths in all Tx–Rx pairs.
- **Reflection coefficient magnitude error (RCM Error):** This metric complements the overall error by specifically

evaluating the prediction accuracy of ray-surface interaction loss. Both predicted and GT values are converted to a logarithmic scale, and the error is computed using NMSE, following the same averaging procedure as in overall error.

- **Average delay error (AvgDelay Error):** This metric assesses the accuracy of power delay profile (PDP) by comparing the predicted and GT average delays (AvgDelays) [18]. For each Tx–Rx pair, the AvgDelay is computed as the power-weighted mean of τ_n , with weights given by the linear-scale received powers $p(a_n)$:

$$\tau_{\text{avg}} = \frac{\sum_n p(a_n) \tau_n}{\sum_n p(a_n)}. \quad (26)$$

The mean absolute error (MAE) between the predicted and GT values of τ_{avg} is then computed and averaged over all Tx–Rx pairs.

- 3) *Baselines:* To verify the effectiveness of GeNeRT, we compare it with two state-of-the-art approaches: WiNeRT in [18] and LWDT in [20].

C. Ablation Experiment

In this subsection, we conduct ablation experiments on key components of the network to assess the effectiveness of the ResNet and the module-wise pre-training. Fig. 7 presents the overall error of GeNeRT under three different network configurations, evaluated on the test set of \mathcal{S}_1 during system-wise end-to-end training with 10 different random seeds, where each configuration is represented by a low-opacity mean line and a high-opacity shaded error band. The three configurations are as follows:

- **Without ResNet:** The skip connections in the network are removed, while the module-wise pre-training is retained. Only the polarization fusion module is active during training.
- **Without Pre-training:** The polarization component prediction module is trained from scratch, with its weights initialized using the Xavier Uniform method. Both the polarization fusion module and the polarization component prediction module are activated.
- **GeNeRT:** The full model proposed in this paper. Only the polarization fusion module is activated, with its weights initialized via module-wise pre-training.

As shown in Fig. 7, GeNeRT consistently achieves the lowest error throughout training, demonstrating the effectiveness of both the ResNet architecture and the module-wise pre-training strategy. Removing either component leads to clear performance degradation. In particular, the absence of pre-training causes significantly higher error and unstable convergence, especially after 160 epochs. The absence of ResNet also results in a noticeable performance drop compared to the full GeNeRT model, though it remains more stable than the model trained without pre-training.

D. Training Area Performance

In this subsection, we evaluate the performance of GeNeRT in the test set of the \mathcal{S}_1 dataset. As shown in Table III, GeNeRT

TABLE III: MPC prediction performance of different approaches under varying humidity levels. Overall Error (Overall Err.) and RCM Error (RCM Err.) are in a logarithmic scale (dB), while AvgDelay Error (AvgDelay Err.) is in nanoseconds (ns).

	S_1 (Dry)			S_2 (Medium Dry)			S_3 (Wet)		
	Overall Err.	RCM Err.	AvgDelay Err.	Overall Err.	RCM Err.	AvgDelay Err.	Overall Err.	RCM Err.	AvgDelay Err.
WiNeRT	-34.55	-22.43	5.84	-28.54	-17.93	10.58	-28.95	-18.61	9.49
LWDT	-38.04	-26.32	3.82	-38.13	-24.93	4.25	-37.46	-23.66	5.10
GeNeRT	-39.71	-27.07	3.43	-39.11	-26.68	3.56	-38.85	-26.62	3.85

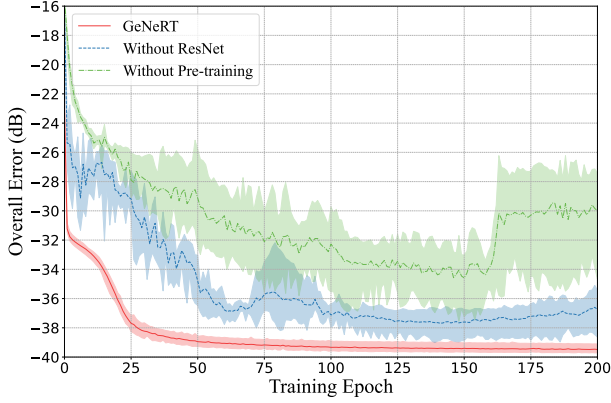


Fig. 7: Ablation experiment

outperforms both WiNeRT and LWDT across all evaluation metrics, demonstrating its superior accuracy in MPC prediction. It is worth noting that the overall error is significantly lower than the RCM error, mainly because it includes free-space propagation loss, which introduces minimal prediction error and dilutes the NMSE. To provide a more intuitive illustration of GeNeRT's ability to predict MPCs, we take three Tx-Rx pairs from the S_1 test set as examples and present their propagation paths, time-domain CIRs, and AvgDelay in Figs. 8 and 9, as well as Table IV, respectively. As shown in Fig. 8, the majority of paths predicted by GeNeRT closely align with those from WI, with only a few exhibiting minor deviations. These deviations consistently occur at the ray's final interaction with the environment, where the absence of the classical mirror-image method slightly perturbs the boundary condition enforcement and leads to sub-wavelength geometric discrepancies. In Fig. 9, the delay values from WI and GeNeRT are nearly identical, except for several single-reflection paths, and the corresponding received power deviation remains within 1.5 dB. Table IV presents a numerical analysis of the PDP deviations for each Tx-Rx pair in Fig. 8 and offers a more intuitive understanding of the AvgDelay error.

TABLE IV: Comparison of AvgDelay between GeNeRT and WI under different Tx-Rx pairs (ns).

	Tx-Rx Pair #1	Tx-Rx Pair #2	Tx-Rx Pair #3
WI	151.21	95.77	119.83
GeNeRT	148.87	95.39	116.43
AvgDelay Err.	2.34	0.39	3.41

E. Adaptability to Environmental Humidity

It is recognized that scatterers belonging to the same semantic class may exhibit diverse EM propagation behaviors

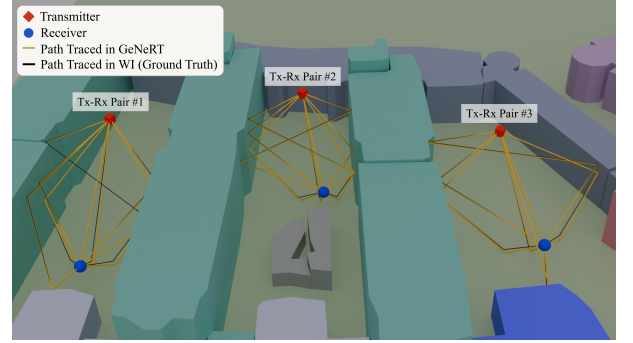


Fig. 8: Propagation path diagram. Propagation paths produced by GeNeRT are generally consistent with those in WI, with certain paths exhibiting exact overlap.

under different humidity conditions. This subsection evaluates the adaptability of GeNeRT to varying humidity levels using the test sets of S_2 and S_3 . Considering that both pre-training datasets S_{\perp} and S_{\parallel} were collected in dry environments, it is necessary to activate the weights in both the polarization component prediction module and the polarization fusion module during system-wise end-to-end training.

As shown in Table III, GeNeRT maintains stable MPC prediction across varying humidity levels. From the dry scenario S_1 to the wet scenario S_3 , the variations in overall, RCM, and AvgDelay errors remain minimal, with respective standard deviations of only 0.43 dB, 0.23 dB, and 0.21 ns. In contrast, baseline methods suffer from noticeable degradation, particularly in AvgDelay error under high humidity. The robust performance of GeNeRT suggests that the system-wise end-to-end training effectively mitigates humidity-induced changes in scatterer characteristics, thereby ensuring reliable MPC prediction under diverse environmental conditions.

F. Generalization Test

In this subsection, we evaluate the generalization capability of different approaches on datasets S_4 to S_{15} . Specifically, S_4 – S_{14} assess intra-scenario spatial transferability, while S_{15} tests inter-scenario zero-shot generalization.

1) *Intra-Scenario Spatial Transferability*: In system-wise end-to-end training, Rx's are positioned within a limited region. This motivates an evaluation of intra-scenario spatial transferability to test the model's generalization to untrained areas. To assess generalization along specific dimensions (e.g., horizontal and vertical) while avoiding confounding factors, we employ two controlled test settings. Datasets S_4 and S_5 vary the Rx's horizontal position at a fixed height, and are used to evaluate horizontal generalization. In contrast, datasets S_6 to S_{14} vary the Rx's height at a fixed horizontal location, and are used to assess vertical generalization.

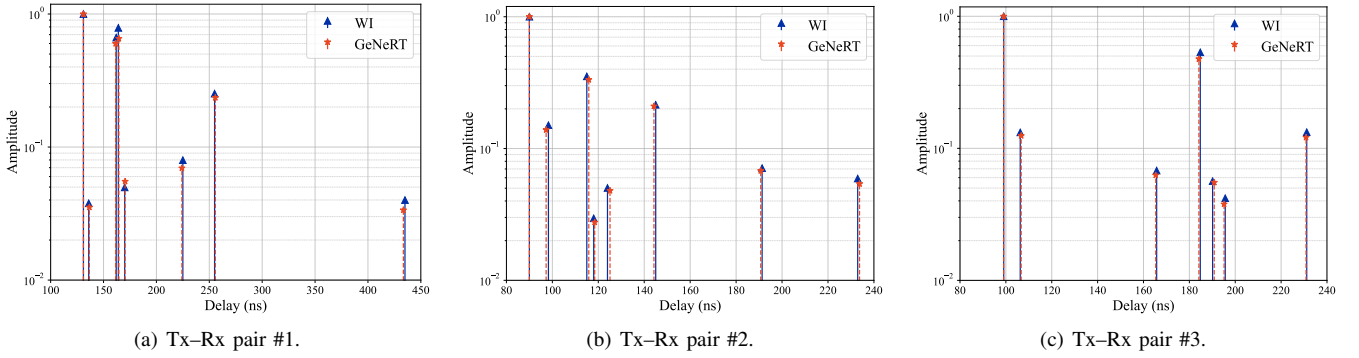


Fig. 9: Comparison of CIRs between GeNeRT and WI under different Tx-Rx pairs.

TABLE V: Predictive performance of different approaches for generalization evaluation. Overall and RCM errors are in dB, while AvgDelay error is in ns.

	\mathcal{S}_4			\mathcal{S}_5			\mathcal{S}_{15}		
	Overall Err.	RCM Err.	AvgDelay Err.	Overall Err.	RCM Err.	AvgDelay Err.	Overall Err.	RCM Err.	AvgDelay Err.
WiNeRT	-22.58	-8.84	28.45	-20.89	-7.14	30.99	-8.92	-3.36	35.18
LWDT	-25.58	-13.01	19.26	-25.07	-11.47	22.35	-10.85	-4.97	32.38
GeNeRT	-37.69	-25.79	3.96	-36.29	-24.69	4.34	-35.36	-23.77	4.91

From the results of \mathcal{S}_4 and \mathcal{S}_5 in Table V, GeNeRT consistently achieves the highest MPC prediction accuracy. When the Rx's horizontal position varies, GeNeRT exhibits only a slight drop across all metrics, while both baselines experience notable performance degradation compared to the training region. As shown in Fig. 10, when the Rx height deviates from the training height, GeNeRT continues to deliver stable performance, maintaining an RCM error of -23.79 dB even at a height difference of 14 m. In contrast, LWDT maintains moderate accuracy at small height differences, but its error gradually increases as the Rx moves higher. WiNeRT is particularly sensitive to vertical changes, showing a sharp increase in error as the height difference grows. These results demonstrate the superior generalization capability of GeNeRT across both horizontal and vertical spatial variations.

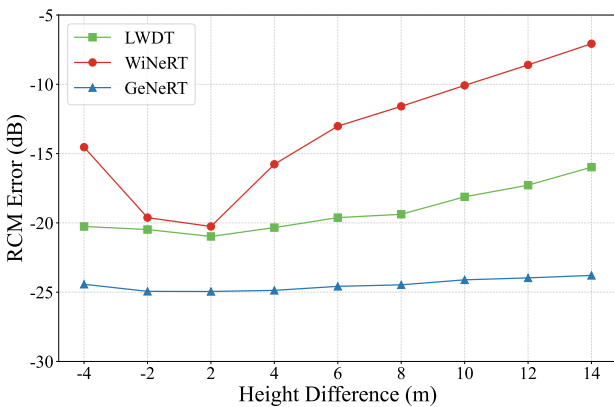


Fig. 10: NMSE of RCM under different Rx heights. The height difference is defined as the test Rx height minus the training Rx height, where a positive value indicates that the test Rx is higher, while a negative value indicates that it is lower.

2) *Inter-Scenario Zero-Shot Generalization Capability:* After evaluating intra-scenario spatial transferability, we con-

sider a more challenging case with entirely different building layouts. In campus environments, different building clusters often share common characteristics, such as materials and architectural styles. A neural RT method that maintains reliable MPC prediction across such clusters can eliminate the need for retraining under scenario changes. As shown in the results of \mathcal{S}_{15} in Table V, GeNeRT consistently maintains superior performance, achieving an overall error of -35.36 dB, an RCM error of -23.77 dB, and an AvgDelay error of only 4.91 ns. In contrast, WiNeRT and LWDT experience substantial degradation, confirming that they struggle to generalize under unseen environments. These results further validate the inter-scenario generalization capability of GeNeRT.

G. Simulation Time Comparison with Conventional RT

In this subsection, we choose WI as a representative of conventional RT methods for simulation time comparison. Specifically, we compare the time overhead of GeNeRT and WI under the \mathcal{S}_{15} dataset configuration. We further examine how different numbers of TxS and RxS affect simulation time by considering four Tx-Rx setups in Scenario 3. The specific settings are summarized in Table VI. While the total number of Tx-Rx pairs remains constant across all setups, the ratio of TxS to RxS varies. For a fair comparison, simulation time is defined as the total duration required to compute the CIR for all Tx-Rx pairs. Both methods are executed on the same server equipped with an AMD EPYC 9654 CPU and an NVIDIA GeForce RTX 4090 GPU. Fig. 11 presents the average simulation time over 100 independent runs under each setup. As observed, when the number of TxS is small (e.g., only one), the simulation time of WI and GeNeRT is comparable. However, as the proportion of TxS increases, GeNeRT exhibits a growing advantage, highlighting its superior runtime efficiency in large-scale multi-Tx scenarios.

TABLE VI: Tx/Rx Count Configurations for different Setups.

Setup	Tx	Rx	Number of Tx-Rx pairs
Setup 1	Tx#1	Multiple Rx #1–8	2352
Setup 2	Tx#1,2	Multiple Rx #1–4	2352
Setup 3	Tx#1–4	Multiple Rx #1,2	2352
Setup 4	Tx#1–8	Multiple Rx #1	2352

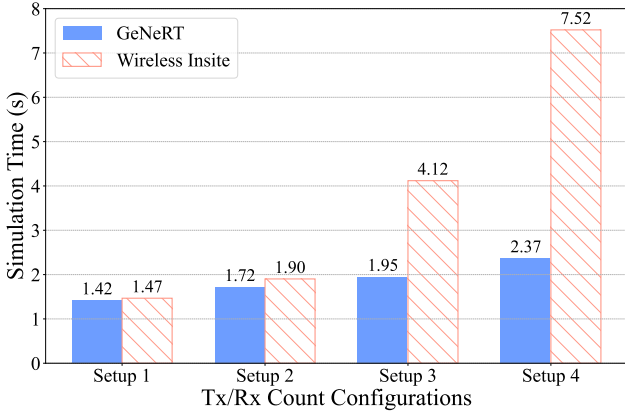


Fig. 11: Comparison of simulation time between GeNeRT and WI.

V. CONCLUSION

In this paper, we propose GeNeRT, a novel neural RT framework that exhibits strong generalization capabilities under limited training data. Built on a neural interaction prediction network and a two-stage training strategy, GeNeRT enables accurate polarization-aware modeling of intrinsic EM propagation mechanisms. Moreover, our framework eliminates the requirement for full path information and supports system-wise end-to-end training based solely on Rx-side delay and AoA. Extensive experiments show that GeNeRT outperforms state-of-the-art baselines in MPC prediction across diverse settings. Specifically, GeNeRT is robust to variations in environmental humidity and exhibits strong intra-scenario spatial transferability as well as inter-scenario zero-shot generalization capability. Additionally, our framework exhibits superior runtime efficiency in large-scale multi-Tx scenarios.

Building upon GeNeRT, future work may consider the following directions:

- **Multiple propagation mechanisms:** Extend the neural interaction prediction network to support more complex propagation mechanisms, such as diffuse scattering and diffraction.
- **Calibration with real-world measurements:** Perform system-wise end-to-end training using CIRs obtained from real-world measurements.
- **More comprehensive and fine-grained classification of scatterer semantics:** Integrate multi-modal information, including images and real-world channel data, to better categorize scatterers with similar EM characteristics.

REFERENCES

- [1] K. Bian *et al.*, “Generalizable neural ray tracing towards physics-informed intelligent channel modeling,” in *Proc. ICCV*, 2025, submitted for review.
- [2] C.-X. Wang *et al.*, “A survey of 5G channel measurements and models,” *IEEE Commun. Surveys Tuts.*, vol. 20, no. 4, pp. 3142–3168, Aug. 2018.
- [3] 3GPP, “Technical specification group radio access network; study on channel model for frequencies from 0.5 to 100 GHz (Release 14),” 3rd Generation Partnership Project (3GPP), TR 38.901 V14.2.0, Sept. 2017. [Online]. Available: <http://www.3gpp.org/DynaReport/38901.htm>
- [4] R. D. Graglia and A. F. Peterson, “Computational electromagnetics and the IEEE antennas and propagation society: Seventy-five years of shared history, part 1,” *IEEE Antennas Propag. Mag.*, vol. 66, no. 5, pp. 16–30, Aug. 2024.
- [5] D. He *et al.*, “The design and applications of high-performance ray-tracing simulation platform for 5G and beyond wireless communications: A tutorial,” *IEEE Commun. Surveys Tuts.*, vol. 21, no. 1, pp. 10–27, Aug. 2019.
- [6] G. Steinböck *et al.*, “Hybrid model for reverberant indoor radio channels using rays and graphs,” *IEEE Trans. Antennas Propag.*, vol. 64, no. 9, pp. 4036–4048, Jul. 2016.
- [7] A. Maltsev *et al.*, “Quasi-deterministic approach to mmWave channel modeling in a non-stationary environment,” in *Proc. IEEE Globecom Workshops (GC Wkshps)*, Dec. 2014, pp. 966–971.
- [8] C. Huang *et al.*, “Artificial intelligence enabled radio propagation for communications—Part II: Scenario identification and channel modeling,” *IEEE Trans. Antennas Propag.*, vol. 70, no. 6, pp. 3955–3969, Feb. 2022.
- [9] E. Zhu *et al.*, “Physics-informed generalizable wireless channel modeling with segmentation and deep learning: Fundamentals, methodologies, and challenges,” *IEEE Wireless Commun.*, vol. 31, no. 6, pp. 170–177, 2024.
- [10] Bakirtzis *et al.*, “Empowering wireless network applications with deep learning-based radio propagation models,” *IEEE Wireless Commun.*, pp. 1–8, Mar. 2025.
- [11] M. Li *et al.*, “DeepRT: A hybrid framework combining large model architectures and ray tracing principles for 6G digital twin channels,” *Electronics*, vol. 14, no. 9, p. 1849, May 2025.
- [12] L. Bai *et al.*, “Multi-modal intelligent channel modeling: A new modeling paradigm via synesthesia of machines,” *IEEE Commun. Surveys Tuts.*, 2025.
- [13] R. Levie *et al.*, “RadioUNet: Fast radio map estimation with convolutional neural networks,” *IEEE Trans. Wireless Commun.*, vol. 20, no. 6, pp. 4001–4015, Feb. 2021.
- [14] A. Gupta *et al.*, “Machine learning-based urban canyon path loss prediction using 28 GHz manhattan measurements,” *IEEE Trans. Antennas Propag.*, vol. 70, no. 6, pp. 4096–4111, Feb. 2022.
- [15] X. Zhao *et al.*, “NeRF²: Neural radio-frequency radiance fields,” in *Proc. ACM MOBICOM*, Madrid, Spain, Oct. 2023, pp. 1–15.
- [16] H. Lu *et al.*, “NeWRF: A deep learning framework for wireless radiation field reconstruction and channel prediction,” in *Int. Conf. on Machine Learning (ICML)*, Vienna, Austria, Jun. 2024, pp. 1–13.
- [17] C. Wen *et al.*, “WRF-GS: Wireless radiation field reconstruction with 3D gaussian splatting,” in *Proc. IEEE INFOCOM*, Feb. 2025, pp. 1–10.
- [18] T. Orekondy *et al.*, “WiNeRT: Towards neural ray tracing for wireless channel modelling and differentiable simulations,” in *Proc. 11th Int. Conf. Learn. Rep.*, Feb. 2023, pp. 1–20.
- [19] Y. Jin *et al.*, “SANDWICH: Towards an offline, differentiable, fully-trainable wireless neural ray-tracing surrogate,” *arXiv preprint arXiv:2411.08767*, 2024.
- [20] S. Jiang *et al.*, “Learnable wireless digital twins: Reconstructing electromagnetic field with neural representations,” *IEEE Open J. Commun. Soc.*, 2025.
- [21] H. Jia *et al.*, “Neural reflectance fields for radio-frequency ray tracing,” in *Proc. IEEE Global Commun. Conf. (GLOBECOM)*, Dec. 2024, pp. 4226–4231.
- [22] M. K. Samimi and T. S. Rappaport, “3-D millimeter-wave statistical channel model for 5G wireless system design,” *IEEE Trans. Microw. Theory and Techn.*, vol. 64, no. 7, pp. 2207–2225, Jul. 2016.
- [23] T. Möller and B. Trumbore, “Fast, minimum storage ray-triangle intersection,” *J. Graph. Tools*, vol. 2, no. 1, pp. 21–28, Sep. 1997.
- [24] J. Hoydis *et al.*, “Sionna RT: Differentiable ray tracing for radio propagation modeling,” in *Proc. IEEE Globecom Workshops (GC Wkshps)*, Dec. 2023, pp. 317–321.
- [25] T. S. Rappaport, *Wireless Communications: Principles and Practice*, 2nd ed. Upper Saddle River, NJ, USA: Prentice-Hall, 2001.
- [26] P. Series, “Effects of building materials and structures on radiowave propagation above about 100 MHz,” Recommendation ITU-R P.2040-1, pp. 2040–1, 2015.